The Astrophysical Journal, 968:118 (16pp), 2024 June 20 https://doi.org/10.3847/1538-4357/ad488a

Large-scale Overdensity of Lyman Break Galaxies around the $z = 6.3$ Ultraluminous Quasar J0100 + 2802

Maria Pudoka[1], Feige Wang[1], Xiaohui Fan[1], Jinyi Yang[1], Jaclyn Champagne[1], Victoria Jones[1], Fuyan Bian[2], Zheng Cai[3], Linhua Jiang[4,5], Dezi Liu[6], and Xue-Bing Wu[4,5]
[1] Steward Observatory, University of Arizona, 933 North Cherry Avenue, Tucson, AZ 85721-0065, USA; pudoka@arizona.edu
[2] European Southern Observatory, Alonso de Cordova 3107, Casilla 19001, Vitacura, Santiago 19, Chile
[3] Department of Astronomy, Tsinghua University, Beijing 100084, People's Republic of China
[4] Department of Astronomy, School of Physics, Peking University, Beijing 100871, People's Republic of China
[5] Kavli Institute for Astronomy and Astrophysics, Peking University, Beijing 100871, People's Republic of China
[6] South-Western Institute for Astronomy Research, Yunnan University, Kunming 650500, People's Republic of China
Received 2023 September 28; revised 2024 May 6; accepted 2024 May 6; published 2024 June 20

Abstract

We study the environment of the $z = 6.33$ ultraluminous quasar SDSS J010013.02+280225.8 (J0100) to understand its association with large-scale structure. Theoretical models propose high-redshift quasars as markers of galaxy overdensities residing in the most massive dark matter halos (DMHs) in the early Universe. J0100 is an ultraluminous quasar with the most massive black hole known at $z \gtrsim 6$, suggesting a high likelihood of residing in a massive DMH. We present wide-field ($\sim$522 arcmin^2) imaging in the *r*, *i*, and *z* bands from the Large Binocular Cameras on the Large Binocular Telescope, with *Y*- and *J*-band imaging from the Wide-field Infrared Camera on the Canada–France–Hawaii Telescope, centered on J0100. Applying color selections, we identify 23 objects as *i*-dropout Lyman break galaxy (LBG) candidates in the J0100 field. We use the deep photometric catalog in the 1.27 deg^2 COSMOS field to calculate the density of LBGs in a blank field, and to estimate the selection completeness and purity. The observed surface density of LBG candidates in the J0100 field corresponds to a galaxy overdensity of $\delta = 4$ (at 8.4σ). This large-scale overdensity suggests that the $\sim$22 arcmin^2 overdensity found by Kashino et al. using JWST data extends out to much larger scales. We calculate the angular autocorrelation function of the candidates and find a positive correlation on $\lesssim 10'$ scales as well as evidence of asymmetries in their spatial distribution, further suggesting the direct detection of large-scale structure in the field of the ultraluminous quasar J0100.

Unified Astronomy Thesaurus concepts: Quasars (1319); Large-scale structure of the universe (902); High-redshift galaxy clusters (2007); High-redshift galaxies (734); Lyman-break galaxies (979)

1. Introduction

Over the last two decades of quasar research, ground-based surveys have unveiled the existence of a large population of luminous quasars at $z \sim 6$; residing well within the epoch of reionization (EOR), these quasars have black hole masses $\geqslant 10^9\ M_\odot$ (Venemans et al. 2013; Wu et al. 2015; Bañados et al. 2016; Jiang et al. 2016; Wang et al. 2019b; Yang et al. 2019, 2021; Fan et al. 2023). These rare quasars, powered by such massive black holes, require that the black holes must have grown to their current state in less than 1 Gyr after the Big Bang. Their formation and subsequent growth in such a short period of time have provoked theoretical exploration into many possible evolutionary scenarios for supermassive black holes (SMBHs; Inayoshi et al. 2020; Volonteri et al. 2021).

Cosmological simulations can produce these SMBHs by $z \sim 6$ by allowing exceptionally high accretion rates (super-Eddington) or starting with massive ($<10^{3-4}\ M_\odot$) seeds. These simulations (Springel et al. 2005; Overzier et al. 2009) along with the highly clustered nature of quasars (Mo & White 2002; Eftekharzadeh et al. 2015) and quasar abundance matching (Lukić et al. 2007) all indicate that these quasars reside in the most massive dark matter halos (DMHs). SMBHs then grow through two essential processes: accreting cold gas and merging with other black holes following the idea of hierarchical structure formation (Haehnelt & Rees 1993; Di Matteo et al. 2005, 2012). The scenarios framing the formation and growth of these quasars suggest that they reside in overdense environments of galaxies as they must (i) reside in the most massive DMHs that typically host clusters, (ii) be surrounded by large reservoirs of gas from which they can accrete, and (iii) be near many other black holes with which they will merge. In the most extreme overdense regions, these galaxy overdensities could eventually settle into galaxy clusters with $M \sim 10^{14-15}\ M_\odot$ by the present day (Costa et al. 2014). The progenitors of these are known as protoclusters.

Galaxy clusters and protoclusters play a significant role in advancing our understanding of the formation and evolution of the Universe. Protoclusters, in particular, provide valuable insights into the growth of early structure formation. The distribution of DMHs on a cosmic scale is theoretically traced by luminous matter: galaxies and protoclusters at high redshifts (Adelberger et al. 2005). Comparing the observed structures and properties of protoclusters at high redshifts to cosmological simulations can also help to test various theories for dark matter or cosmological initial conditions (see Overzier 2016 for a review). Additionally, the high star formation rates in these early structures (Costa et al. 2014; Chiang et al. 2017) likely played a role in carving out bubbles of ionized hydrogen during the EOR, opening a window to constrain the ionizing radiation

field of early galaxies and the topology of reionization (Whitler et al. 2024). Furthermore, probing the galaxy properties in these dense environments at such early stages can shed light on galaxy formation and evolution, particularly how these differ from galaxy formation and evolution in more typical, less dense regions (Lee-Brown et al. 2017; Nantais et al. 2017).

Though theory predicts overdense regions around high-redshift quasars (Overzier et al. 2009; Romano-Diaz et al. 2011), there have been mixed results when it comes to observations of the environments of these quasars (Kim et al. 2009). Some authors have reported overdensities of galaxies in quasar environments (Kashikawa et al. 2007; Utsumi et al. 2010; Balmaverde et al. 2017) while others have found no significant evidence of an overdensity (Willott et al. 2005; Bañados et al. 2013; Mazzucchelli et al. 2017), and in some cases, even underdense environments have been reported (Simpson et al. 2014). Many hypotheses have been proposed to account for these inconsistencies. As discussed below, these include small fields of view (FOVs), strong quasar feedback, and differing selection techniques.

Overdensities anchored by quasars at $z \sim 6$ should easily extend to several tens of comoving megaparsecs (cMpc) away from the central quasar (Overzier et al. 2009; Chiang et al. 2013). These distances correspond to FOVs as large as $\sim 30' \times 30'$ at $z \sim 6$. Many searches use deep imagers with FOVs on the order of only a few arcminutes on a side, corresponding to $\lesssim$10 cMpc at $z \sim 6$ (Stiavelli et al. 2005; Kim et al. 2009; Simpson et al. 2014; Mazzucchelli et al. 2017). Using these small FOVs can lead to missing many galaxies that are part of the structure, thus diluting the overdensity signal. Another plausible explanation includes powerful quasar feedback heating the intergalactic medium (IGM) on scales up to a few comoving megaparsecs (Babul & White 1991; Scannapieco & Oh 2004). This ionizing radiation can prevent star formation (at least in the lowest-mass galaxies) and reduce the ability to observe Lyα emitters (LAEs) or Lyman break galaxies (LBGs) tracing the dark matter overdensities near the quasar (e.g., Utsumi et al. 2010). It is evident that varying sizes of the FOV can severely affect the detection of an overdensity (Chiang et al. 2013).

Another difficulty with drawing conclusions based on the results of these studies arises from the fact that various groups use different selection techniques. Some authors search for submillimeter galaxies (Champagne et al. 2018; Meyer et al. 2022) or [O III] emitters (Kashino et al. 2023; Wang et al. 2023), while others look for LBGs or LAEs (Bañados et al. 2013; Morselli et al. 2014; Balmaverde et al. 2017; Mignoli et al. 2020; Champagne et al. 2023). Some fields even show conflicting results depending on which type of galaxy is selected (e.g., Ota et al. 2018). This occurred also in Utsumi et al. (2010) and Goto et al. (2017) in which an overdensity of LBGs was initially detected and a follow-up search for LAEs resulted in no overdensity. It is clear that the search for dark matter overdensities traced by biased galaxy populations is heavily reliant on both observational constraints and the chosen galaxy selection.

With the launch of JWST, there have been a number of efforts within the past year to search for [O III] emitters in the fields of massive quasars using JWST's deep NIRCam wide-field slitless spectroscopic capabilities. Though the FOV is small (two $2.2' \times 2.2'$ detectors), the initial findings of these probes into $z \sim 6$ quasar environments have found many instances of galaxy overdensities. For example, Kashino et al. (2023) surveyed a $6.5' \times 3.4'$ area around J0100+2802 and found 24 [O III]-emitting systems exactly at the redshift of the quasar, many more than those at foreground redshifts from the quasar. Additionally, Wang et al. (2023), discovered a filamentary structure consisting of the luminous quasar J03053150 and 10 [O III] emitters at $z = 6.6$ making this an overdensity of $\delta = 12.6$ in an FOV of one NIRCam pointing. The strength of JWST in probing the faint end of the galaxy overdensity is evident, but ground-based searches for bright galaxies over much wider fields are still valuable to detect the full spatial extent of the overdensities.

In this study, we analyze the $\sim 58 \times 58$ cMpc^2 (or $\sim 8 \times 8$ physical Mpc^2 at $z = 6.33$) field around the ultraluminous quasar SDSS J010013.02+280225.8 (J0100). J0100 is the most luminous quasar powered by the most massive black hole identified at $z \gtrsim 6$ (Wu et al. 2015). With a luminosity of $L_{\rm bol} \sim 10^{48}$ erg s^{-1} (Wu et al. 2015), a black hole mass of $M_{\rm BH} \sim 10^{10}$ $M_\odot$ (Eilers et al. 2023), and a host galaxy mass of $M_{\rm dyn} \geqslant 7 \times 10^{10}$ $M_\odot$ (Wang et al. 2019a), it is an ideal candidate to reside in a massive DMH capable of hosting a galaxy overdensity. Our analysis uses data from the Large Binocular Camera (LBC) on the Large Binocular Telescope (LBT) and the Wide-field Infrared Camera (WIRCam) on the Canada–France–Hawaii Telescope (CFHT). These instruments provide a simultaneously wide and deep optical and near-infrared (NIR) imaging of the quasar field with an FOV of $\sim 25' \times 23'$ in the r, i, z, Y, and J filters.

As mentioned, an overdensity of [O III] emitters has been detected within an area of $6.5' \times 3.4'$ centered on J0100 using JWST/NIRCam slitless spectroscopy (Kashino et al. 2023). While this spatial scale probes out to roughly 7 cMpc away from the quasar, we alternatively focus on selecting LBGs as tracers of the large-scale structure of dark matter on scales up to $\sim$25 cMpc away from the quasar. Our objective is to investigate the large-scale environment at protocluster scales using the photometric i-dropout technique discussed in Section 3.

The structure of this paper is as follows. In Section 2, we describe the observations, data reduction, and the photometric catalog used for the subsequent analysis. Section 3 discusses the selection criteria for the LBG candidates including filtering out contaminants. Section 4 describes the calculation of the expected number of LBGs in a blank field and the completeness and contamination of the sample. In Section 5, we present the evidence for the existence of a galaxy overdensity and examine the spatial distribution of the high-redshift candidates. Finally, in Section 6, we summarize our findings. All magnitudes are reported in the AB system and we adopt a Lambda cold dark matter (ΛCDM) cosmology in which $H_0 = 70$ km s^{-1} Mpc^{-1}, $\Omega_{\rm m} = 0.3$, and $\Omega_\Lambda = 0.7$ in which $1'' = 40.6$ ckpc at $z = 6.3$.

2. Observations and Data Reduction

2.1. LBT and CFHT Observations

For this analysis, observations were taken using the LBCs on the LBT along with additional data from the WIRCam on the CFHT. The observation designs are described below.

The LBCs are two wide-field imagers mounted on the prime focus of the LBT. The LBC Blue is optimized for observations from 3500 Å to 6500 Å, while the LBC Red is optimized for

observations from 5500 Å to 1 μm. Both cameras have an FOV of $\sim 25' \times 23'$ (Giallongo et al. 2008; Speziali et al. 2008). The LBC observations were obtained on 2015 November 22 (UT) under clear conditions (PI: X. Fan). To enable the *i*-dropout selection, we observed the J0100 field with the $i_{\rm SDSS}$ and $z_{\rm SDSS}$ filters on the red channel of LBC. Additionally, we obtained $r_{\rm SDSS}$ imaging on the blue side of LBC simultaneously. The individual exposures for all images were set to 100 s to minimize the effects from cosmic rays and the saturation of bright stars in the field. The total on-source exposure in *r* band, *i* band, and *z* band are 3.7 hr, 1.5 hr, and 2.1 hr, respectively.

Furthermore, we performed NIR imaging with WIRCam on CFHT for J0100 (PI: J. Yang, RunID: 17BS03). The WIRCam is a wide-field imager and has an FOV of $\sim 21.5' \times 21.5'$ (Puget et al. 2004). Taking advantage of the large FOV, the WIRCam observations could fully cover the FOV of each LBC with a carefully designed dithering pattern. Following Balmaverde et al. (2017), we selected the *Y* and *J* broadband filters for this program. The data have been obtained in Queue mode through the Telescope Access Program of NAOC[7] during the 2017B semester. The individual exposures for the *Y* band and *J* band were 120 s and 60 s, respectively. In total, we integrated 6.0 hr and 6.9 hr for *Y* band and *J* band, respectively. To improve the sampling, we used both the standard dithering and microdithering[8] (with a 2×2 microstepping pattern) for our observations.

2.2. Photometric Data Reduction

We process the data using a custom data reduction pipeline named `PyPhot`.[9] `PyPhot` includes the standard imaging data reduction processes including bias subtraction, flat-fielding, and sky background subtraction.

For the LBC images, the master bias and flat are generated by finding the sigma-clipped median on a series of bias and sky flats, respectively. For the *i* and *z* bands, we further correct fringing by subtracting off a master fringe frame constructed from our science exposures. The sky background is estimated using `SourceExtractor` (Bertin & Arnouts 1996) after masking out bright stars. Cosmic rays are masked using the Laplacian edge detection algorithm (van Dokkum 2001).

For the WIRCam images, we start with the preprocessed individual image data delivered by CFHT (dark subtracted, flat-field corrected, and with preliminary background subtraction). A detailed description of the detrending of these images can be found on the CFHT WIRCam image detrending webpage.[10] These detrended images are then processed with `PyPhot` for further background subtraction, bad pixel masking, and cosmic-ray rejection as was done for the LBC images.

For each of these data sets, the final mosaic is produced using `SCAMP` (Bertin 2006) and `Swarp` (Bertin et al. 2002). Additionally, a mask is created in order to remove saturation spikes and bright foreground stars in the images. The effective clean area of the coadded and masked LBC mosaic is 0.153 deg^2 and that of the WIRCam mosaic is 0.181 deg^2. Additionally, the pixel scale of the final mosaics are 0.″224 pixel^{-1} and 0.″153 pixel^{-1} for the LBC and WIRCam images, respectively.

Table 1
Summary of Observational Information Used in This Study

Filter	Central Wavelength (Å)	Exposure Time (hr)	3σ Depth (mag)
r	6200	3.7	26.55
i	7670	1.5	26.38
z	9608	2.1	25.79
Y	10240	6.0	25.65
J	12518	6.9	25.26

2.3. Photometric Calibration and Catalog Creation

We perform object detection on each mosaic with `SourceExtractor` by setting `DETECT_THRESH = 1.5` and `DETECT_MINAREA = 4`. To calibrate the photometric measurements, the individual exposures for LBC and WIRCam are calibrated to the Pan-STARRS (Chambers et al. 2016) and Two Micron All Sky Survey (2MASS; Skrutskie et al. 2006) infrared photometric catalogs, respectively. We only use sources that have been detected in all five Pan-STARRS bands. We further require that the difference between the `Kron` magnitude and `PSF` magnitude in the Pan-STARSS catalog are smaller than 0.3 mag in all five bands and have a signal-to-noise ratio (S/N) greater than 10 with no FLAGS from `SourceExtractor` in our data. Finally, we restrict these points to be in the magnitude range of $18 < {\rm mag} < 20$ in Pan-STARRS and $15.5 < {\rm mag} < 17.5$ in 2MASS to ensure the strongest correlation in magnitudes. This results in $\sim$250 sources for the Pan-STARRS calibration and $\sim$150 sources for the 2MASS calibration.

Using these bright point sources, we calibrate the zero-points for each filter using color terms derived from standard stars. To check the reliability of our calibrations, we compare our magnitudes against the reference magnitudes obtained from the Pan-STARRS and 2MASS photometric catalogs after applying color corrections for the bright stars. We find that the standard deviations of the differences between our magnitudes and the reference magnitudes is 0.05, 0.06, 0.05, 0.15, and 0.09 for the *r*, *i*, *z*, *Y*, and *J* bands, respectively. This photometric accuracy is highly adequate for high-redshift Lyman break selections.

We then merge the catalogs of all sources detected in the five bands by assuming that objects with distance greater than 1.″0 are unique sources as the seeing for the LBT observations is around 1.″0. Finally, we perform forced aperture photometry for all unique objects with `Photutils` (Bradley et al. 2021). The exposure times and magnitude limits with a 2.″0 diameter aperture of the fully calibrated images are listed in Table 1.

3. Lyman Break Galaxy Candidate Selection

The Lyman break technique is an effective way to search for star-forming high-redshift galaxies due to the drastic decrease in flux observed at wavelengths blueward of the Lyα line ($\lambda_{\rm Ly\alpha} = 1216$ Å). This drop in flux, due to the increasing neutral hydrogen fraction of the IGM before the end of cosmic reionization causing photons with energies higher than Lyα to be absorbed, is known as the Gunn–Peterson trough (Gunn & Peterson 1965). At redshifts $z \geqslant 5$, this break in the spectra, usually seen in the ultraviolet (UV), is shifted into the NIR.

[7] https://tap.china-vo.org
[8] https://www.cfht.hawaii.edu/Instruments/Imaging/WIRCam/specsinformation.html
[9] https://github.com/PyPhot/PyPhot
[10] https://www.cfht.hawaii.edu/Instruments/Imaging/WIRCam/IiwiVersion2Doc.html

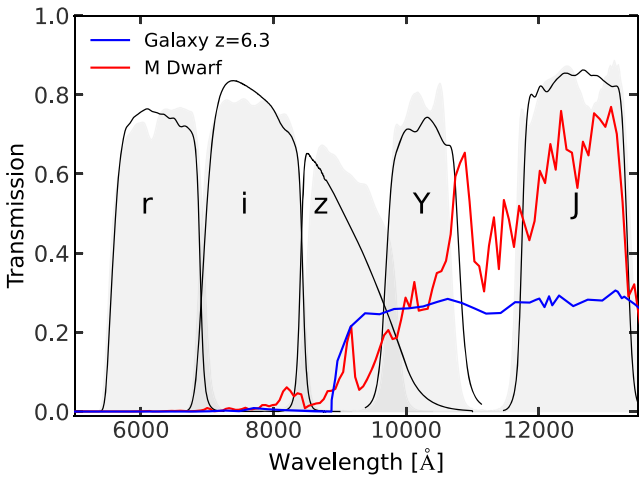

Figure 1. In black are the transmission curves of the LBT/LBC r, i, and z filters and of the CFHT/WIRCAM Y and J filters. A template of a young star-forming galaxy redshifted to $z = 6.3$ with IGM absorption taken into account (Inoue et al. 2014) is shown in blue with $(i-z,\ z-Y,\ z-J) = (3.85,\ 0.77,\ 0.82)$. An M-type dwarf stellar template is shown in red (Allard et al. 2012) with $(i-z,\ z-Y,\ z-J) = (2.37,\ 1.50,\ 2.67)$. The gray, filled curves show the filter curves of the corresponding COSMOS data described in Section 4.

Specifically, at the redshift of J0100, Figure 1 shows the Lyman break of a galaxy template shown in blue at a wavelength of $\lambda_{\rm obs} = 8877$ Å, which falls in the Sloan Digital Sky Survey (SDSS) z filter on the LBT.

We use the Lyman break technique to select high-redshift galaxy candidates because it provides an effective selection criterion on photometric color rather than relying on many hours of spectroscopic observations. However, as shown in Figure 1 in red, this can be contaminated significantly by late-type M, L, and T dwarfs that have such red colors that they can appear to be dropouts. Below, we explain the color criteria used to select these dropouts along with the color requirements and visual inspection procedure used to remove stellar and other contaminants.

3.1. Color–Color Diagram

The following criteria are used as a preliminary selection of LBG candidates at $z \sim 6$:

$$z_{\rm APER} \leqslant 25.23 \text{ and } ({\rm S/N})_z > 5, \quad (1)$$

$$({\rm S/N})_r < 2, \quad (2)$$

$$i - z > 1.5. \quad (3)$$

The first two criteria, Equation (1), require that the source must be detected in the z band to 5σ and have an S/N of greater than 5 in this band. We use the $2\farcs0$ diameter aperture photometry for this cut, however, after further inspection, using the `MAG_AUTO` magnitudes as other searches have done (e.g., Morselli et al. 2014; Balmaverde et al. 2017) does not change the results of this selection significantly. The third criterion, Equation (2), constrains the selection to sources not detected significantly in the r band as the IGM absorption should be fully saturated at these wavelengths.

Finally, as can be seen by the vertical line in Figure 2, the color selection in Equation (3) favors sources whose Lyman break falls at redshifts above $z \sim 5.6$. It has been shown that this is an efficient color cut for selecting starburst galaxies near redshift six (Stanway et al. 2003; Bowler et al. 2015). For context, Figure 2 also shows color tracks of a star-forming galaxy template simulated by the Flexible Stellar Population Synthesis (Conroy et al. 2009; Conroy & Gunn 2010) and retrieved from the `EAZY` code (Brammer et al. 2008; Brammer 2021). These tracks are shown for redshifts between 5.5 and 6.4 as gray lines.

It is evident that we expect a nondetection in the i-band filter. To account for this nondetection, for any source that has less than a 2σ detection in this filter, we use the 2σ magnitude limit of $m_i = 26.82$ as an upper limit to the corresponding sources in the i band. This upper limit is used in calculating the $i-z$ colors and results in a lower limit in the $i-z$ colors (i.e., the true color is more red). Even with the upper limit on the i-band magnitude, combining the first and fourth criteria means that it will still be eligible for color selection. One caveat to consider is that extremely deep i-band imaging is needed to rule out $z = 5.7$ galaxies from the overdensity. We cannot definitively conclude that the overdensity is at the quasar's redshift or a redshift of 5.7, therefore, we aim to attain spectroscopic follow-up of these galaxy candidates in the future.

After these four selection criteria are applied, 149 sources remain. Many of which are low-redshift contaminants or spurious artifacts (e.g., bright star halos, saturation spikes, and cosmic rays). We also acknowledge that this color selection can result in a large redshift range (5.7–6.5) possibly probing galaxies that are not actually part of the same structure. This is due to the use of broadband photometric filters. However, Overzier et al. (2009) showed that galaxy protoclusters can span up to 100 cMpc, which corresponds to a window of roughly $\Delta z \sim 0.3$ centered on the quasar's redshift. Thus, it is still possible that galaxies with a slight redshift offset are still within the same overdense structure. Additionally, a positive angular correlation of LBGs, even in a wide redshift window, can be used as evidence for being part of the same structure as is described in Section 5.

3.2. Removal of Contaminants

As mentioned above, low-mass stars, brown dwarfs, and Balmer break galaxies at $z \sim 1.5$ can contaminate this selection due to their extremely red colors (Bowler et al. 2015). Figure 1 shows a comparison between a galaxy template at a redshift of $z = 6.3$ in blue and an M-dwarf star in red. It can be seen that this cool star has minimal flux in the r and i filters with some flux in the z band similar to i-dropouts.

With the additional data given by the Y and J bands from the CFHT, it is possible to remove most of these targets as they should appear much redder in the $z-Y$ and $z-J$ colors. Figure 2 shows stars in the J0100 observations as green dots. These are selected with the `SourceExtractor` parameter `CLASS_STAR` > 0.98 and a magnitude limit of $z_{\rm AUTO} < 23$. As expected, these points generally populate a different color space than the color tracks of galaxies.

This separation can also be seen as the green track in Figure 2 which shows the typical colors of MLT dwarfs based on the Sonora model atmosphere grid (Marley et al. 2021). The diagonal lines in Figure 2 show the relative color cut utilized to remove stellar contamination. These cuts are optimized with the COSMOS data set (Weaver et al. 2022), which provides a much larger set of stars determined with a higher confidence due to the many filters included in the COSMOS survey. To be conservative while determining these cuts, we prioritize the purity of the sample over the completeness considering a high

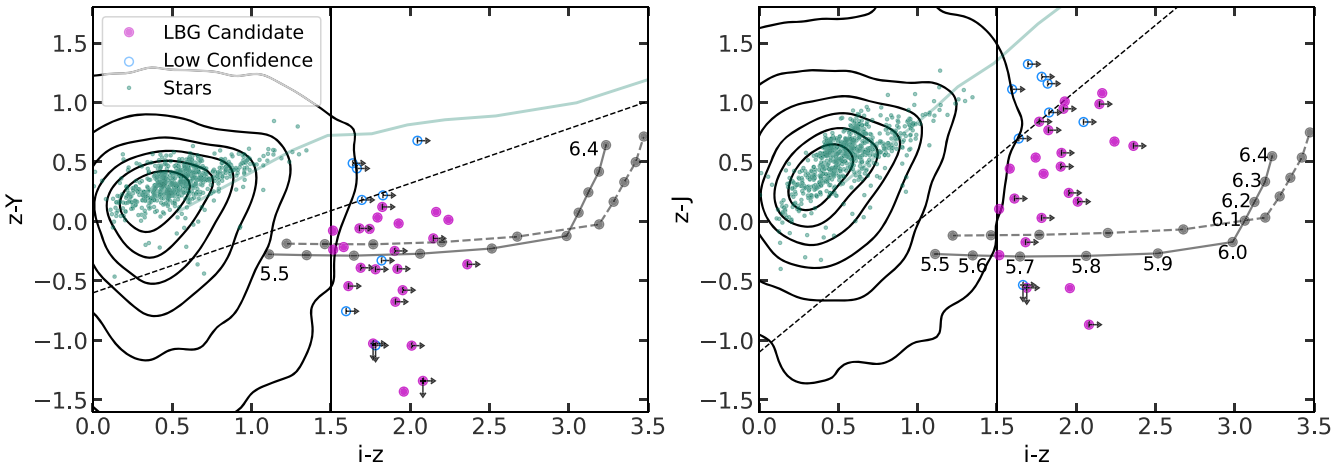

Figure 2. Color–color diagrams with LBG candidates (filled magenta points), low-confidence candidates (open blue circles), and stellar sources (green points) in the field. These show the $z-Y$ (left) and $z-J$ (right) colors vs. the $i-z$ color. The vertical line shows the color cut at $i-z<1.5$ while the diagonal dotted line shows the cut to remove stellar contaminants. The gray tracks in each plot show the theoretical colors of a young star-forming galaxy at redshifts ranging from $z=5.5$ to $z=6.4$ at redshift intervals of $\Delta z=0.1$. The black contours show the region where all sources detected in the J0100 field reside. The green track shows theoretical colors of solar-metallicity MLT dwarfs calculated using the Sonora model grid (Marley et al. 2021). Arrows on the pink and blue points show lower(upper) limits on the $i-z$ ($z-Y/J$) colors due to nondetections in the i, Y, or J bands. Note, many of these candidates have true $i-z$ colors that are more red than portrayed.

contamination fraction could result in a false overdensity signal. To parameterize this cut, we first fit a line to the COSMOS stellar sources in the color–color plane. Then the y-intercept is shifted far enough below the stellar locus to remove the majority of COSMOS stellar sources from the selection. With this in mind, these diagonal cuts on the $z-Y$ and $z-J$ colors removed 99.8% of the sources that are flagged as stars in the COSMOS catalog. The following diagonal cuts are applied to the remaining 149 candidates from Section 3.1:

$$z-J<1.10(i-z)-1.1, \tag{4}$$

$$z-Y<0.46(i-z)-0.6. \tag{5}$$

After eliminating stellar-like objects with the intersection of these two cuts (i.e., both $z-Y$ and $z-J$ below the cut), 68 candidates are ready for visual inspection. Due to the depth of the i-band filter, there are some sources that do not meet this color criterion but could be pushed out of the disallowed region due to the lower limit on the $i-z$ color. Thus, we provide a low-confidence sample of possible LBG candidates that have a lower limit in the $i-z$ color, and have $z-Y$ or $z-J$ below the cut, and $J>23.5$. This results in an additional nine low-confidence sources to be visually inspected.

Visual inspection is required due to spurious sources and other image artifacts such as bright star halos and saturation spikes being incorrectly identified as sources by `SourceExtractor`. An example of the result of this visual inspection can be seen in Figure 3 where the top row shows a valid LBG candidate, the middle row shows a stellar source (that was removed through the cuts of the $z-Y/J$ colors), and the bottom row shows a saturation spike erroneously extracted by `SourceExtractor`.

After visual inspection to remove extended sources and other defect/noise sources, 23 galaxies remain with an additional eight low-confidence sources. Thus, we discover 23 LBG candidates around J0100 in an area of $\sim$500 arcmin^2, all of which can be seen in Figure 4. Their coordinates and magnitudes are tabulated in Appendix A and the cutouts in each filter are shown in Appendix B at the end of this paper. The additional low-confidence sources can be found at the bottom of the same table. These low-confidence sources are not included in the calculations of overdensity or clustering that follow.

Of the 23 main candidates and eight low-confidence candidates, none of them overlap with the Kashino et al. (2023) [O III] emitters in the same field. In Matthee et al. (2023), in which these [O III] emitters are characterized, the representative UV magnitude is $M_{\rm UV}=-19.6\pm0.1$ for the full sample and $M_{\rm UV}=-19.5\pm0.1$ for the [O III] emitters at $z>6.25$. At the assumed redshift, this corresponds to an apparent magnitude of $m_{\rm UV}\sim27.2$, which is below the detection thresholds for our study. Therefore, we do not expect to detect these as LBG candidates from our data. Furthermore, the LBG candidates found here fall outside of the smaller FOV of the JWST observations at larger spatial scales.

3.3. Spectral Energy Distribution Fitting

We calculate the photometric redshifts with two codes—`LePhare`[11] (Arnouts et al. 1999; Ilbert et al. 2006) and `EAZY`[12] (Brammer et al. 2008; Brammer 2021)—in order to compare the χ^2 values between the galaxy and stellar templates. Both programs fit spectral templates to the observed $2\farcs0$ aperture fluxes of each source. For `EAZY`, we use the 17 templates adopted by Weaver et al. (2022) with a uniform redshift prior. `LePhare` uses both 31 galaxy templates (Ilbert et al. 2009) and 254 stellar spectral energy distributions (Pickles 1998; Chabrier et al. 2000). The redshifts have large uncertainty due to the broad filters and small number of filters used. However, the stellar fit χ^2 values are indeed all larger than those for the galaxy fits indicating that these are likely high-redshift galaxies as opposed to low-mass stars within the Galaxy.

It is worth noting that Kashino et al. (2023) found several overdensities of [O III] emitters with slight redshift offsets from J0100. It is necessary for spectroscopic follow-up to determine if these candidate LBGs reside in the environment of the quasar

[11] https://www.cfht.hawaii.edu/~arnouts/LEPHARE/lephare.html
[12] https://github.com/gbrammer/eazy-py

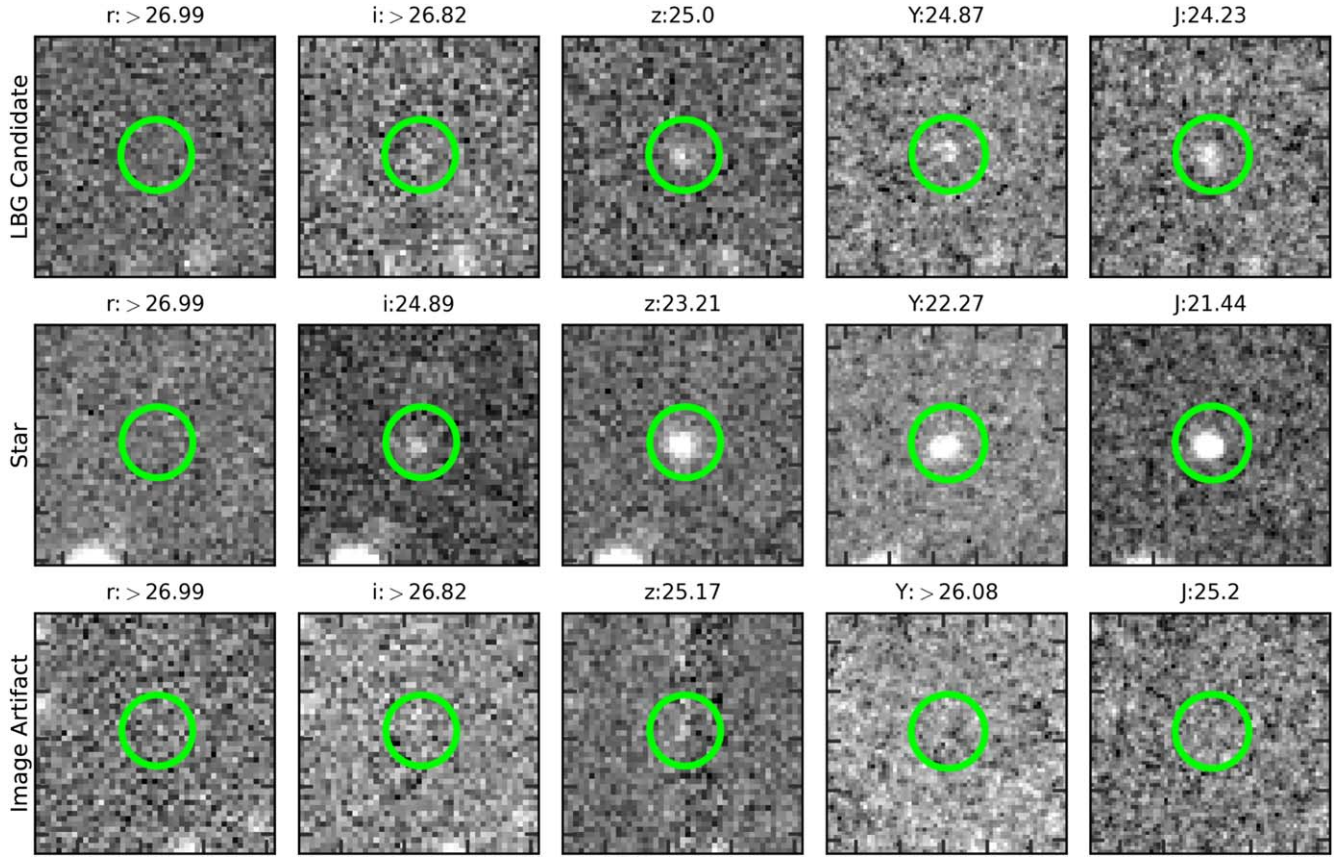

Figure 3. Examples of the visual inspection process using $10'' \times 10''$ cutouts of each source in the *r*, *i*, *z*, *Y*, and *J* bands. Each cutout is independently normalized to a stretched Z-scale interval. The top row displays a promising LBG candidate that passes visual inspection, the middle row shows a stellar source, and the bottom row shows an image artifact that is not a true source.

or in foreground overdensities. Mignoli et al. (2020) have done this type of spectroscopic follow-up with LBGs found around another $z = 6.3$ quasar, J1030+0524, in Balmaverde et al. (2017) using similar selection criteria as this paper. Spectra were taken of 12 of the candidate LBGs confirming nine high-redshift galaxies with three undetermined redshifts due to low spectral resolution and a lack of emission lines. Thus, this selection has been proven to be robust and can be confidently used to find high-redshift LBGs. Overall, all candidate galaxies are unlikely to be low-redshift contaminants based on the stellar χ^2 values.

4. Blank Field Comparison with COSMOS

The number of selected LBG candidates in the 0.153 deg^2 LBT field around J0100 is 23. In order to put this number into context, we calculate the number of dropout galaxies in a large blank field using the same selection techniques. We take advantage of the COSMOS field from Weaver et al. (2022), which provides a large amount of photometric data. We apply the `COMBINED` flag ensuring that the sources in this area are covered by UltraVISTA, Suprime-Cam (SC), and Hyper Suprime-Cam along with being free of edges and bright stars. This results in a total area of 1.27 deg^2, which is large enough to represent a field governed by cosmic variance rather than any single overdensity at redshift 6. Not only does this choice benefit from the large area of the COSMOS field, but it is also covered by a large selection of filters.

4.1. Blank Field Lyman Break Galaxy Surface Density

In order to make a comparable selection of *i*-dropout galaxies in the COSMOS field, it is necessary to choose filters that are the most similar to the LBT and CFHT filters used in this paper with depths that are similar to or deeper than our data. We choose the *r*, *i*, and *z* filters from Subaru's SC and the *Y* and *J* filters from VIRCAM on the VISTA telescope. These filters and their respective 3σ depths are shown in Figure 1 and Table 2. The SC *z* band has a similar depth to our data and therefore is ready to be used in the analysis. However, the SC *r* and *i* bands are about a half magnitude deeper than this study. Thus, it is necessary to degrade the COSMOS data in order to match the data quality of this paper.

To fulfill this requirement, we match the background flux limits of the COSMOS data with that of the LBT data in each filter. We convert the SC 3σ magnitude limit to a flux limit for each filter and subtract this value in quadrature from the original flux errors of the SC sources. Next we add in quadrature the 3σ flux limit of the LBT filters to the errors. With this done, the distributions of errors in the relevant flux range ($0.1-1$ μJy) are the same between the COSMOS and LBT data. To degrade the flux values, we add a Gaussian distributed noise term to the fluxes with mean zero and standard deviation of $\sigma = \sqrt{\sigma^2_{\mathrm{LBT,sky}} - \sigma^2_{\mathrm{COS,sky}}}$, where $\sigma_{*,\mathrm{sky}}$ are the 3σ flux depths of the images. From here, we convert back to magnitudes in order to proceed with the same candidate selection as described in Section 3. Figure 5 shows the distribution of *z* magnitudes, the detection filter, for each field.

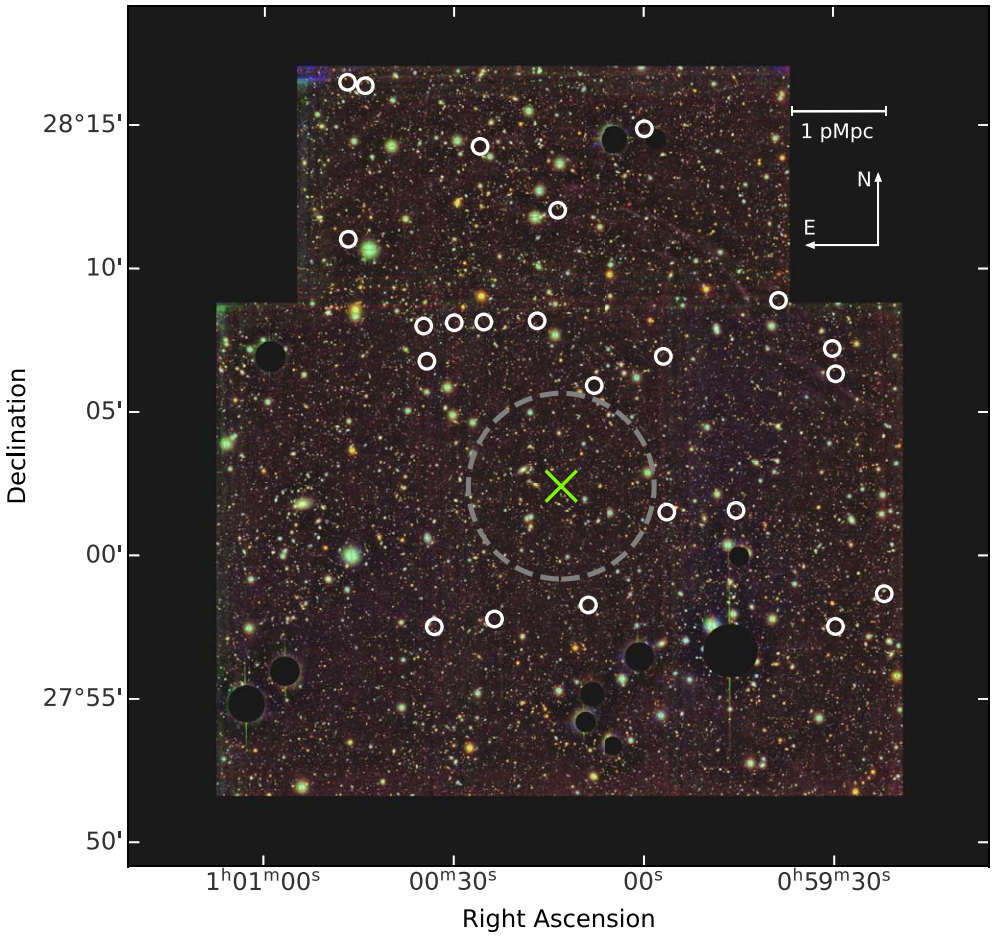

Figure 4. Spatial distribution of candidate LBGs shown as white circles superimposed on a composite color image of the quasar field. The quasar location is marked with a green cross. The field spans an $\sim 23' \times 25'$ area with the majority of the candidate LBGs located in the northwest region of the environment. The gray dashed circle shows a region with a radius of 9 cMpc (1.2 pMpc) in which no LBG candidates are found.

Table 2
Selected COSMOS Catalog Information: the Source Telescope, Central Wavelength, and 3σ Depths for Each Filter of the COSMOS Data Used as a Comparison to the LBT Data

Filter	Source	Central Wavelength (Å)	3σ Depth (mag)
r	Subaru/SC	6305	27.1
i	Subaru/SC	7693	26.7
z	Subaru/SC	8978	25.7
Y	VISTA/VIRCAM	10216	25.3
J	VISTA/VIRCAM	12525	25.9

Note. Y and J depths are for the Deep observations (not UltraDeep) stripes in the COSMOS field.

After following the same selection analysis—which involves the color selections for redshift ($i-z$) and contaminants ($z-Y$ and $z-J$), visual inspection, and photometric redshift calculations—we detect 34 i-dropout galaxy candidates in the whole COSMOS field. That is, we expect 0.007 LBGs per square arcminute.

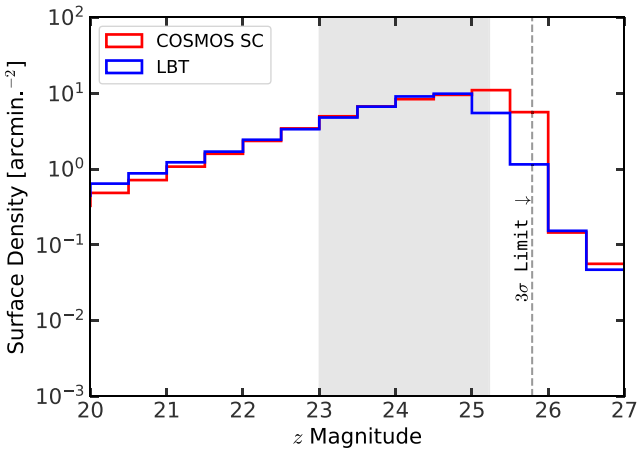

Figure 5. Surface density per square arcminute of the total number of sources detected in the z band in the LBT field (blue) and the COSMOS field (red). The shaded gray region shows the magnitude range of interest within which there is excellent agreement in completeness between the two fields, showing that it is appropriate to use the COSMOS field as a comparison for the overdensity calculation.

4.2. Completeness and Purity

One benefit of using the COSMOS field is the ability to check the completeness and contamination fraction of our selection using the published photometric redshifts in the catalog. COSMOS uses over 20 filters ranging from the UV to NIR to fit to galaxy templates using `EAZY` and `LePhare`. This

abundance of filters allows for a more accurate photometric redshift to be determined. We use the photometric redshifts from the full COSMOS data set as a proxy of the true spectroscopic redshifts, and compare the results to the selection using data degraded to match the LBT/WIRCam data set.

Using the full COSMOS data set, we find 48 galaxies with photometric $z > 5.5$ to a flux limit of $z_{\rm AB} = 25.23$. Of these 48 high-redshift galaxies, we select 17 objects using degraded data following the same selection criteria. Thus, the completeness of our selection technique is 35.4% meaning there could be up to 60 more LBGs in the environment of the quasar at this flux limit.

Promisingly, of the 34 LBG candidates selected by the degraded COSMOS data using only five filters, 50% of them (17) are designated true high-redshift galaxies with the COSMOS redshifts, while others are low-redshift interlopers due to the degraded data quality. This 50% contamination rate indicates that at least 13 candidates in the J0100 field are true high-redshift galaxies in the environment of the quasar.

5. Overdensity and Structure of Lyman Break Galaxies around J0100

5.1. Overdensity Measurement

The overdensity of galaxies in a portion of the sky is determined by the equation:

$$\delta = \frac{n}{\bar{n}} - 1. \tag{6}$$

In this equation, $\bar{n}$ is the average number of galaxies in a blank field where no overdensity is expected and n is the number of galaxies actually detected in the area of the quasar.

To calculate the number of candidates from the COSMOS field expected in a field size of the LBT FOV, we randomly point a box with the same dimensions of the LBT FOV at the COSMOS field 10,000 times. For each pointing, the number of the 34 selected LBG candidates from the COSMOS field within the area is recorded. We fit a Gaussian function to the distribution of these counts and recover a mean galaxy count of 4.6 with a standard deviation of 2.2. The distribution of these pointings is shown in Figure 6 where the red vertical line shows the number of candidate galaxies in the J0100 field.

It is evident that there is a significant overdensity in the field around J0100. The contamination rate does not affect this calculation, because the expected number of LBGs, $\bar{n}$, is calculated from degraded COSMOS data with the same effect. Specifically, with the expected counts, we calculate an overdensity of $\delta = (23/4.6) - 1 = 4$ at 8.4σ significance in the field of J0100.

5.2. Spatial Distribution and Angular Correlation

As the photometric redshifts derived using the EAZY code with only five filters have large uncertainty, it is not reliable to map this protocluster in 3D space using our data. Rather, the calculation of the 2D two-point angular autocorrelation function (ACF) can indicate clustering on an angular scale. If the overdensity is due to a chance alignment of galaxies along the line of sight, one would expect to see no angular clustering above that of a blank field. However, if the galaxies within the protocluster are truly associated with one another, one would expect them to be strongly clustered.

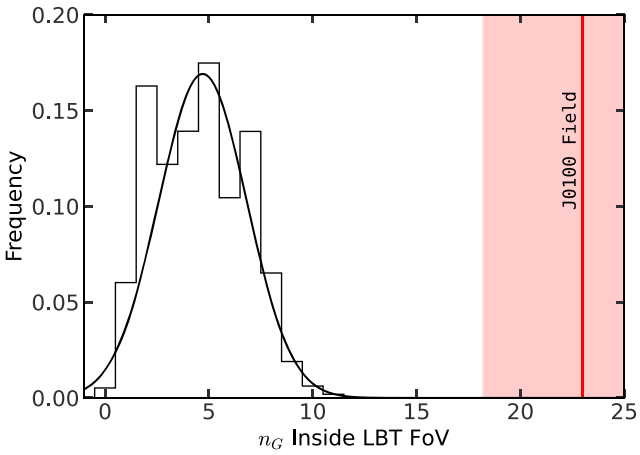

Figure 6. Frequency histogram of the number of LBGs counted in an LBT FOV-sized box after 10,000 Poisson pointings within the COSMOS field. The thick black line is a Gaussian fit to the data with $\mu = 4.6$ and $\sigma = 2.2$. The red vertical line shows the number of LBG candidates counted in the J0100 field while the red shaded region shows the Poisson error on this count.

Figure 4 shows the distribution of the LBG candidates in the field and highlights the need for large FOVs as there are no LBG candidates within 9 cMpc (diameter of 7.4′) from the quasar. Using single pointings from the Hubble Space Telescope's Advanced Camera for Surveys (∼3.4′ × 3.4′) or JWST's NIRCam (∼2.2′ × 5.1′), one would, at best, not capture the full extent of the galaxy overdensity, and at worst, not detect it at all.

Additionally, it is evident from Figure 4 that many of the galaxy candidates reside in the northwest portion of the imaging field. To ensure that this is not due to sensitivity variations in the different chips on the detector or other sky variations, we calculate the number counts from the original catalog with quality cuts in each quadrant of the image. The results show that while the total catalog and clean catalog show the same distribution of sources in each quadrant (roughly 25% as expected), the candidate distribution does not. Running a two-sample Z-test between the percentage of sources in the northwest quadrant from the catalog and that of the candidates shows that there is only a 1.1% chance that there would be this large of a fraction of candidates in this quadrant compared to the original distribution of sources in the image. This indicates that the asymmetry of the candidate distribution is not likely due to the distribution of the original catalog.

To evaluate this structure in a more quantitative way, we use the two-point angular ACF, which calculates the likelihood of finding a galaxy within a given angular distance of another galaxy compared to what would be expected from a randomly distributed population. To measure this, we use the Landy & Szalay (1993) correlation function estimator, which is used in many galaxy correlation studies (Lee et al. 2006; Overzier et al. 2006; McLure et al. 2009; Wang et al. 2013). This takes the form of:

$$\omega(\theta) = \frac{\widehat{DD} - 2\widehat{DR} + \widehat{RR}}{\widehat{RR}}. \tag{7}$$

$\widehat{DD}$, $\widehat{DR}$, and $\widehat{RR}$ are the normalized pair counts between real galaxies, between real galaxies and random points, and between random points, respectively, residing within separations of $\theta + \Delta\theta$. These are calculated with the raw number of

galaxy–galaxy, galaxy–random, and random–random pairs (*DD*, *DR*, and *RR*, respectively), the number of data sources (n_d), and the number of random points (n_r) as follows:

$$\hat{DD} = \frac{DD}{n_d(n_d - 1)/2}, \tag{8}$$

$$\hat{DR} = \frac{DR}{n_d n_r}, \tag{9}$$

$$\widehat{RR} = \frac{RR}{n_r(n_r - 1)/2}. \tag{10}$$

We use a random distribution made up of 10,000 mock sources that fit within the same geometry of the LBT field. This takes into account the mask used to remove areas around saturated stars and other noisy regions used during the selection process. We investigate the span of separations between $1' - 30'$. These angular separations correspond to ∼2−75 cMpc at the redshift of the quasar, thus probing the protocluster to its outermost regions (Overzier et al. 2009). We use logarithmic binning of these separations in order to sufficiently sample the pairs at small separations while avoiding unnecessarily fine binning at large angular separations as seen in Figure 7.

The ACFs for both the 23 LBG candidates and for stellar sources in the LBT field are shown in Figure 7 in black and red, respectively. Errors were determined using the Poisson estimator:

$$\Delta\omega(\theta) = \frac{1 + \omega(\theta)}{\min(N_{\rm pair}, N_{\rm data})^{1/2}}, \tag{11}$$

as described in Croom et al. (2005) and da Ângela et al. (2005). The galaxy candidates show a positive clustering signal at separations of less than $10'$. The stellar sources in the field, determined by CLASS_STAR $\geqslant 0.98$, show essentially no clustering signal as expected for a random distribution of stars in the FOV.

We assume a power-law ACF in the form $\omega_{\rm obs}(\theta) = \omega_{\rm true}(\theta) - {\rm IC} = A_\omega\theta^{-\beta} - {\rm IC}$ in which the observed ACF signal is skewed downward due to the finite geometry of the field (Roche & Eales 1999). The integral constraint (IC) is used to fit for this underestimation of the clustering signal and is calculated using:

$$\mathrm{IC} = \frac{\sum RR(\theta)\theta^{-\beta}}{\sum RR(\theta)}. \tag{12}$$

The resulting correction used is IC = 0.018. We fit the data using this formula and taking $\beta = 0.6$ as is used in many clustering analyses (Lee et al. 2006; Overzier et al. 2006). The resulting amplitude for the galaxy candidate distribution is $A_\omega = 15 \pm 2\ \mathrm{arcsec}^{0.6}$ and for the stellar distribution $A_\omega = 1.1 \pm 0.2\ \mathrm{arcsec}^{0.6}$. Lee et al. (2006), Overzier et al. (2006), and Harikane et al. (2016) determined the clustering of *i*-dropout galaxies at $z \sim 6$ in the GOODS fields and found clustering amplitudes of 2.71 ± 2.05, $1.12^{+0.34}_{-0.25}$, and 2.7 ± 1.3, respectively, for the bright galaxies in their samples. These are an order of magnitude smaller than that of the galaxies in this study. This strengthens the evidence that these candidate LBGs in the J0100 field come from the same overdense structure.

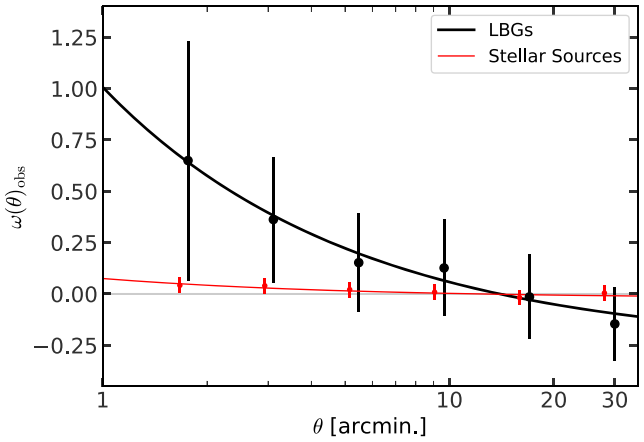

Figure 7. Angular ACF of the 23 LBG candidates in the J0100 field (black points) along with the same for the stellar contaminants shown as red points. Solid lines represent the power law ($\beta = 0.6$) fits to the data with $A_{\omega,\rm LBG} = 15$ and $A_{\omega,\rm stellar} = 1.1$.

5.3. Results in Context

Similar searches for LBGs on ∼10 Mpc scales around $z \sim 6$ quasars have been conducted with similar results (see, e.g., Utsumi et al. 2010; Morselli et al. 2014; Balmaverde et al. 2017; Ota et al. 2018). Each study reports at least slightly overdense quasar fields revealing that searches on these large scales may provide a less biased view into the large-scale structure around quasars. Additionally, those studies that applied extra photometric constrains (e.g., Utsumi et al. 2010 use the z_R filter; Balmaverde et al. 2017 use the *Y* and *J* bands) report slightly higher overdensities. For example, Morselli et al. (2014) looked at the J1030+0524 field only using the *r*, *i*, and *z* bands and found an overdensity of $\delta = 2.0$; however, Balmaverde et al. (2017) expanded upon this search with the *Y* and *J* bands and calculated an overdensity of $\delta = 2.4$ with more confidence of contamination removal. J0100, having a black hole mass roughly 10 times that of J1030+0524 (De Rosa et al. 2011), has a slightly higher overdensity using extremely similar selection techniques. This could indicate a possible correlation with black hole mass, though a much larger sample with spectroscopic confirmation is needed for this assertion.

The LBG candidates in each study are also distributed asymmetrically in the quasar fields. The quasars are not necessarily found at the centers of these overdensities nor are they in the most dense regions. Additionally, all of the observed quasar fields show a lack of LBG candidates in the direct vicinity of the quasar itself. Utsumi et al. (2010), Morselli et al. (2014), and Balmaverde et al. (2017) all report either no or very few LBGs within 1−3 pMpc (7−21 cMpc at $z \sim 6$). Similarly, we find no LBG candidates within 1.2 pMpc (9 cMpc) from J0100. These values are on the order of the sizes of the proximity zones around quasars: the point where the Lyα transmission drops below 10% (Fan et al. 2006). This indicates possible suppression of star formation in galaxies near the quasar due to UV radiation from the quasar heating the IGM causing faint galaxies to dominate at regions closest to the quasar.

It is evident from these results, and those prior, that quasars are likely to live in overdense regions traced by LBGs. While their properties are similar, their exact values (such as

overdensity estimate, clustering signal, and proximity to the quasar) fill a range of parameter space that is still unconstrained.

6. Summary and Conclusion

We utilize the wide-field ($\sim 23' \times 25'$) imaging in the r, i, and z bands from the LBCs on the LBT along with complementary Y and J band imaging from the WIRCam on the CFHT to inspect the large-scale environment around the ultraluminous quasar J0100. This quasar is the most massive known quasar at $z \geqslant 6$, making it an ideal region of space to search for large-scale structure traced by galaxies. The spatial scales probed by this wide field of view correspond to an $\sim 50 \times 50$ cMpc^2 region, the expected extent of large protoclusters from simulations.

We construct a catalog of sources in this field and utilize magnitude-, S/N-, and color-based selection thresholds to identify i-dropout LBGs. We find 23 high-confidence LBGs in the field while only 4.6 LBGs are expected in a region the size of the LBT FOV according to the COSMOS field matched to the data characteristics of our survey. This gives rise to a measured overdensity of $\delta = 4$ at 8.4σ significance. The candidate LBGs show clustering ($A_\omega = 15 \pm 2$ arcsec$^{0.6}$) an order of magnitude larger than foreground stellar sources furthering the evidence of large-scale structure around J0100.

Spectroscopic follow-up will be required on these candidate LBGs to determine their true redshifts and certify whether or not they are truly forming a large-scale structure around J0100.

Acknowledgments

M.P., F.W., and X.F. acknowledge support from NSF grant AST-1908284 and AST-2308258.

This research uses data obtained through the Telescope Access Program (TAP), which has been funded by the Strategic Priority Research Program "The Emergence of Cosmological Structures" (grant No. XDB09000000), National Astronomical Observatories, Chinese Academy of Sciences, and the Special Fund for Astronomy from the Ministry of Finance.

Based on observations obtained with WIRCam, a joint project of CFHT, Taiwan, Korea, Canada, and France, at the Canada–France–Hawaii Telescope (CFHT), which is operated from the summit of Maunakea by the National Research Council of Canada, the Institut National des Sciences de l'Univers of the Centre National de la Recherche Scientifique of France, and the University of Hawaii. The observations at the Canada–France–Hawaii Telescope were performed with care and respect from the summit of Maunakea, which is a significant cultural and historic site.

The LBT is an international collaboration among institutions in the United States, Italy, and Germany. LBT Corporation partners are The University of Arizona on behalf of the Arizona university system; Istituto Nazionale di Astrofisica, Italy; LBT Beteiligungsgesellschaft, Germany, representing the Max-Planck Society, the Astrophysical Institute Potsdam, and Heidelberg University; and The Ohio State University and The Research Corporation, on behalf of The University of Notre Dame, University of Minnesota, and University of Virginia.

Software: NumPy (Harris et al. 2020), Pandas (McKinney 2010, 2011), Matplotlib (Hunter 2007), Astropy (Astropy Collaboration et al. 2013, 2018), SciPy (Virtanen et al. 2020), EAZY (Brammer et al. 2008), LePHARE (Arnouts et al. 1999; Ilbert et al. 2006), Corrfunc (Sinha & Garrison 2020), and Healpy (Zonca et al. 2019).

Appendix A
All Lyman Break Galaxy Candidate Properties

The following Table A1 reports the information of the 23 LBG candidates along with the information for the additional eight low-confidence LBG candidates.

Table A1
Lyman Break Galaxy Candidate Photometry: The Coordinates and 2.″0 Aperture Magnitudes of Each of the 23 LBG Candidates in Our Sample

ID	R.A.	Decl.	r	i	z	Y	J
14812	00:59:22.05	+27:58:40.42	>26.99	>26.82	24.81 ± 0.17	25.85 ± 0.57	24.64 ± 0.26
25390	00:59:29.68	+28:06:20.60	>26.99	>26.82	25.00 ± 0.17	24.87 ± 0.18	24.23 ± 0.14
13026	00:59:29.77	+27:57:32.16	>26.99	25.76 ± 0.20	24.18 ± 0.08	24.39 ± 0.10	23.74 ± 0.09
26465	00:59:30.20	+28:07:13.51	>26.99	26.57 ± 0.43	24.83 ± 0.15	24.89 ± 0.17	24.29 ± 0.14
28643	00:59:38.69	+28:08:54.29	>26.99	>26.82	25.14 ± 0.21	25.20 ± 0.19	25.31 ± 0.30
19190	00:59:45.43	+28:01:35.11	>26.99	>26.82	25.13 ± 0.20	25.52 ± 0.27	>25.69
19112	00:59:56.38	+28:01:31.74	>26.99	>26.82	24.87 ± 0.17	25.45 ± 0.25	24.63 ± 0.17
26129	00:59:56.91	+28:06:57.30	>26.99	>26.82	25.04 ± 0.21	25.44 ± 0.24	25.01 ± 0.24
36179	00:59:59.89	+28:14:53.37	>26.99	>26.82	24.67 ± 0.13	24.82 ± 0.17	23.69 ± 0.10
24874	01:00:07.84	+28:05:56.37	>26.99	>26.82	24.46 ± 0.11	24.82 ± 0.15	23.82 ± 0.08
14197	01:00:08.76	+27:58:17.56	>26.99	>26.82	24.74 ± 0.13	>26.08	25.61 ± 0.42
33271	01:00:13.61	+28:12:03.02	>26.99	26.43 ± 0.37	24.92 ± 0.16	24.99 ± 0.17	24.81 ± 0.20
27691	01:00:16.86	+28:08:11.82	>26.99	>26.82	25.05 ± 0.19	>26.08	24.22 ± 0.11
13448	01:00:23.58	+27:57:48.18	>26.99	26.68 ± 0.47	24.52 ± 0.11	24.44 ± 0.10	23.44 ± 0.06
27635	01:00:25.29	+28:08:09.21	>26.99	>26.82	24.91 ± 0.17	25.59 ± 0.26	24.34 ± 0.12
35552	01:00:25.88	+28:14:16.47	>26.99	>26.82	24.92 ± 0.16	25.17 ± 0.22	24.46 ± 0.17
27638	01:00:29.96	+28:08:07.76	>26.99	25.62 ± 0.21	24.10 ± 0.09	24.34 ± 0.08	24.39 ± 0.13
12974	01:00:33.08	+27:57:31.84	>26.99	26.38 ± 0.39	24.42 ± 0.12	25.85 ± 0.36	24.98 ± 0.23
25887	01:00:34.28	+28:06:47.10	>26.99	>26.82	24.90 ± 0.18	25.30 ± 0.20	23.95 ± 0.09
27460	01:00:34.79	+28:08:00.80	>26.99	26.63 ± 0.50	24.39 ± 0.11	24.38 ± 0.09	23.72 ± 0.07
37982	01:00:44.07	+28:16:23.24	>26.99	26.45 ± 0.49	24.52 ± 0.13	24.54 ± 0.17	23.51 ± 0.10
32277	01:00:46.73	+28:11:02.16	>26.99	>26.82	25.21 ± 0.21	25.75 ± 0.31	25.02 ± 0.23

Table A1
(Continued)

ID	R.A.	Decl.	r	i	z	Y	J
38109	01:00:46.88	+28:16:30.54	>26.99	26.15 ± 0.42	24.35 ± 0.12	24.32 ± 0.15	23.95 ± 0.16
			Low-confidence Sources				
7456	00:59:35.55	+27:53:49.84	>26.99	>26.82	24.99 ± 0.17	24.77 ± 0.19	24.08 ± 0.14
32924	01:00:09.07	+28:11:42.97	>26.99	>26.82	25.22 ± 0.21	25.98 ± 0.41	24.11 ± 0.11
35445	01:00:11.73	+28:14:09.58	>26.99	>26.82	25.18 ± 0.21	24.69 ± 0.15	24.49 ± 0.17
34296	01:00:16.06	+28:13:03.00	>26.99	>26.82	25.03 ± 0.18	25.33 ± 0.24	23.84 ± 0.09
10255	01:00:23.97	+27:55:38.41	>26.99	>26.82	25.13 ± 0.20	24.94 ± 0.18	23.8 ± 0.09
33372	01:00:37.53	+28:12:09.23	>26.99	>26.82	25.15 ± 0.20	24.71 ± 0.12	>25.69
25884	01:01:04.20	+28:06:45.70	>26.99	>26.82	24.77 ± 0.15	24.10 ± 0.12	23.94 ± 0.14
23393	01:01:05.40	+28:04:47.87	>26.99	>26.82	25.04 ± 0.20	>26.08	23.82 ± 0.113

Note. Entries containing a ">" symbol represent nondetections of the source and are depicted as the 2σ upper limit for the corresponding filter. The bottom eight sources are the low-confidence candidates described in Section 3.2

Appendix B
All Lyman Break Galaxy Candidate Cutouts

The following figures (Figures B1–B4) show the postage stamp cutouts of each candidate LBG selected in this study.

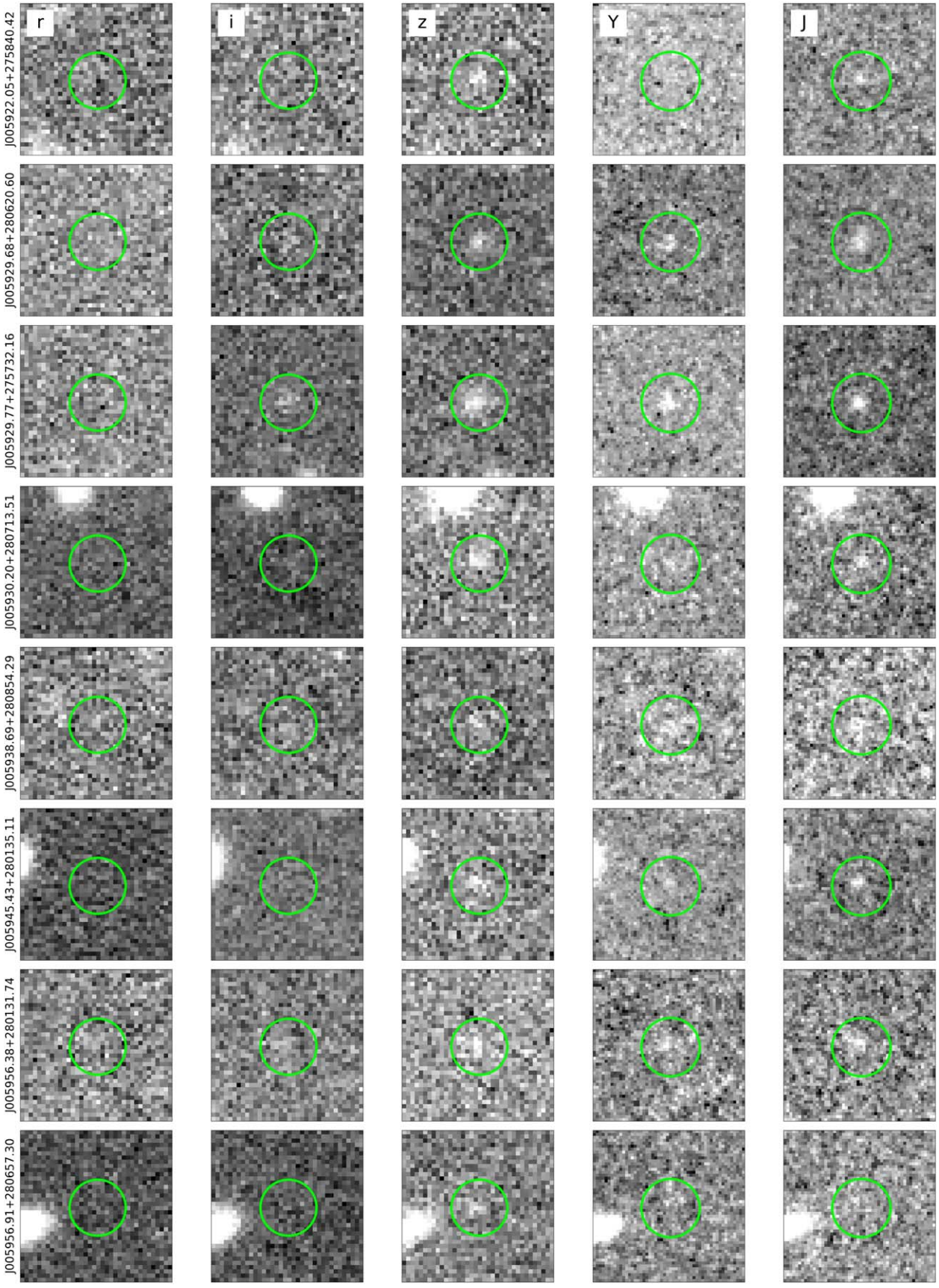

Figure B1. Postage stamp cutouts of each high-confidence candidate LBG listed in Appendix A. These show a 8×8 arcsec^2 cutout centered on each target. The green circles are to aid the eye and have diameters of $3''$.

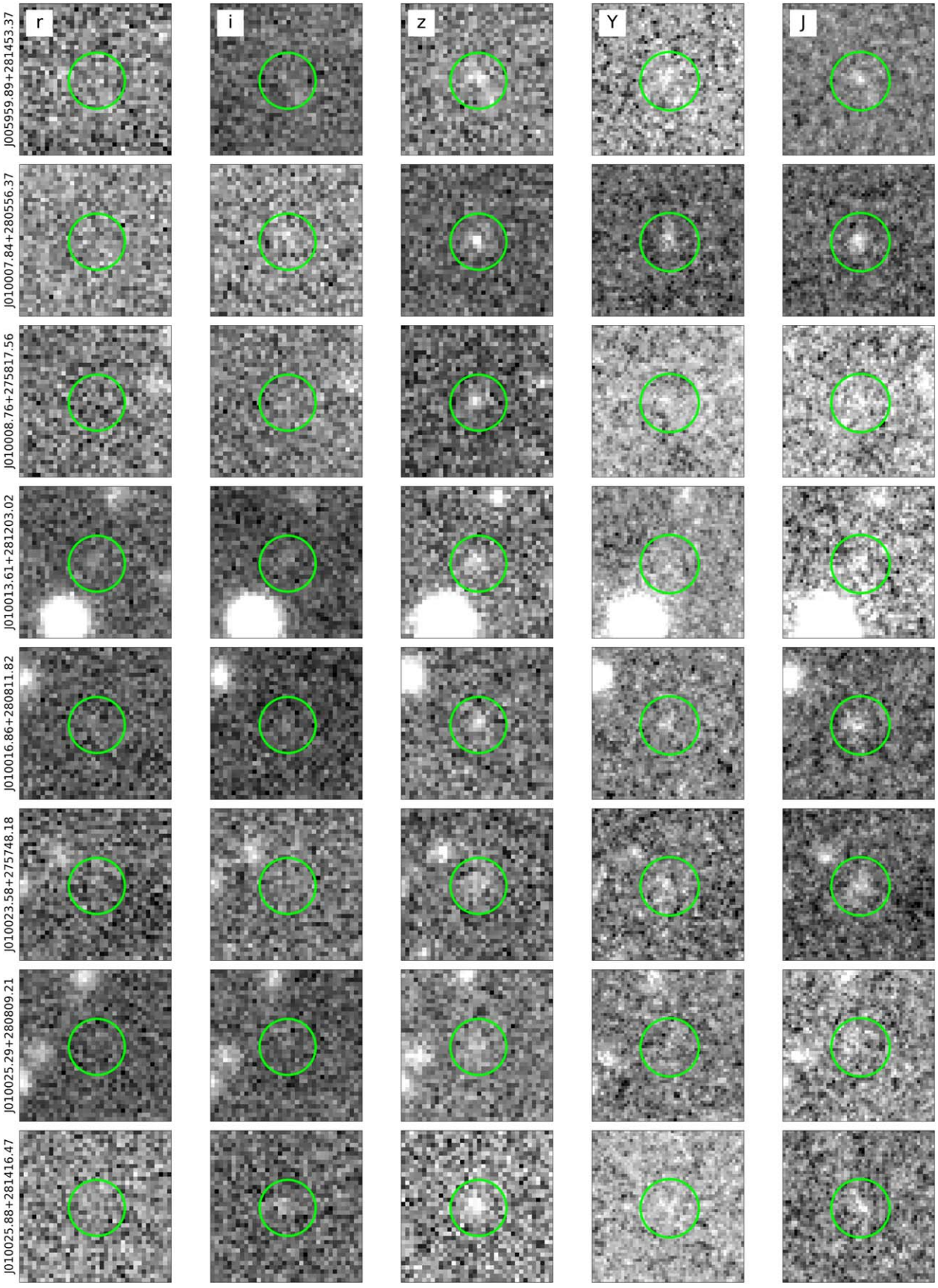

Figure B2. A continuation of Figure B1.

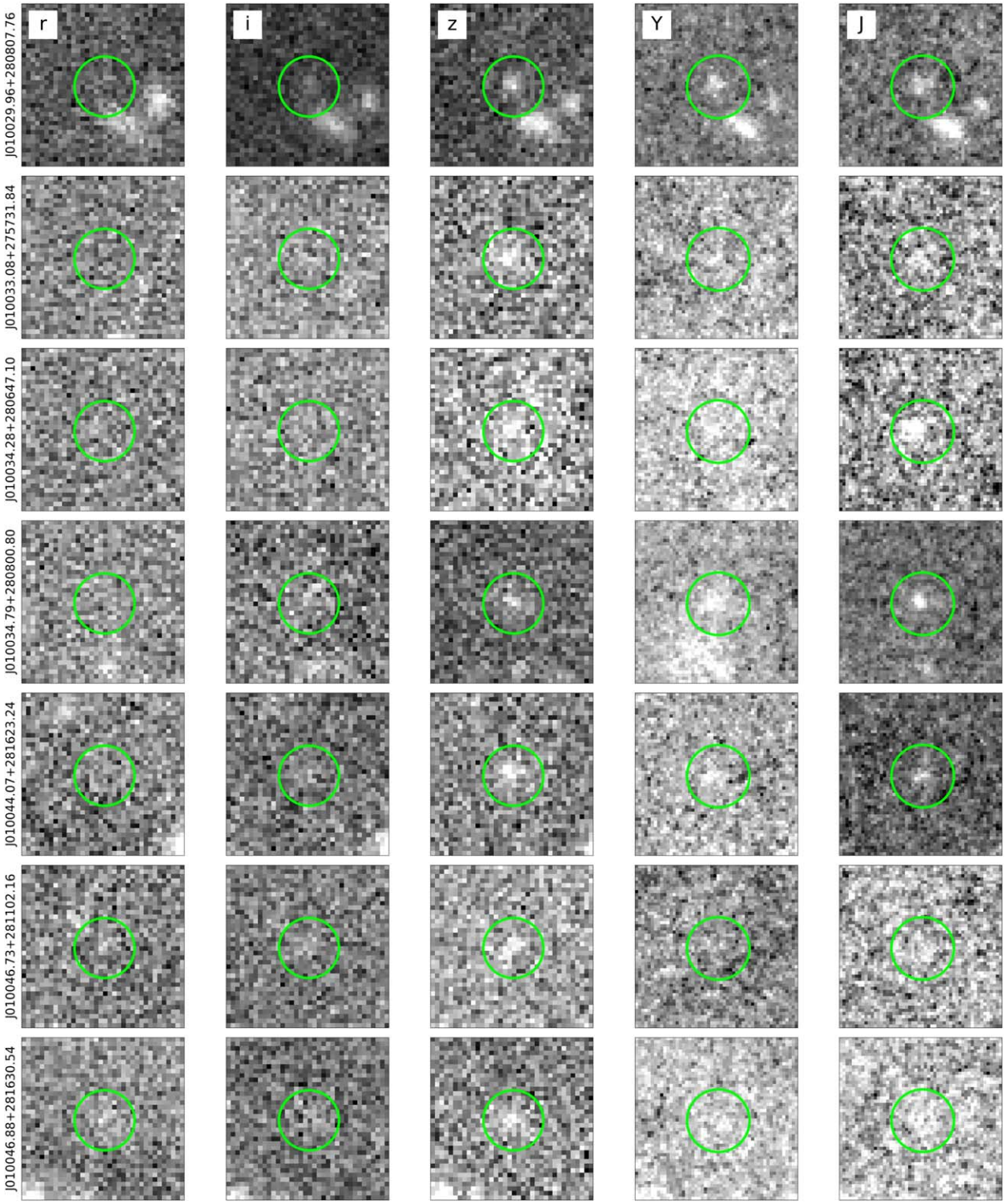

Figure B3. A continuation of Figure B1.

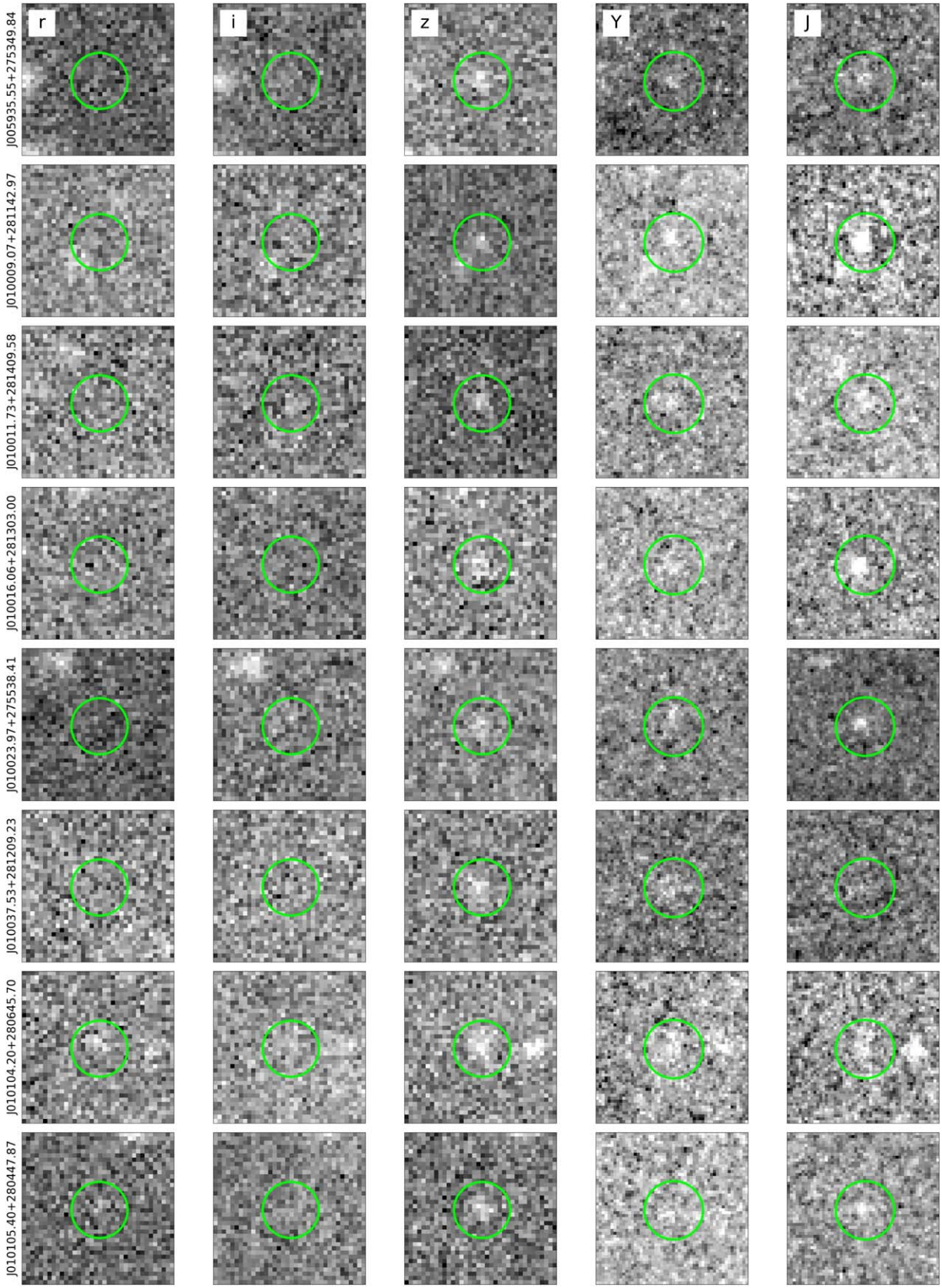

Figure B4. Continuation of Figure B1, but showing the low-confidence targets listed in Table A1.

ORCID iDs

Maria Pudoka https://orcid.org/0000-0003-4924-5941
Feige Wang https://orcid.org/0000-0002-7633-431X
Xiaohui Fan https://orcid.org/0000-0003-3310-0131
Jinyi Yang https://orcid.org/0000-0001-5287-4242
Jaclyn Champagne https://orcid.org/0000-0002-6184-9097
Zheng Cai https://orcid.org/0000-0001-8467-6478
Linhua Jiang https://orcid.org/0000-0003-4176-6486
Dezi Liu https://orcid.org/0000-0002-0409-5719
Xue-Bing Wu https://orcid.org/0000-0002-7350-6913

References

Adelberger, K. L., Steidel, C. C., Pettini, M., et al. 2005, ApJ, 619, 697
Allard, F., Homeier, D., & Freytag, B. 2012, RSPTA, 370, 2765
Arnouts, S., Cristiani, S., Moscardini, L., et al. 1999, MNRAS, 310, 540
Astropy Collaboration, Price-Whelan, A. M., Sipőcz, B. M., et al. 2018, AJ, 156, 123
Astropy Collaboration, Robitaille, T. P., Tollerud, E. J., et al. 2013, A&A, 558, A33
Babul, A., & White, S. D. M. 1991, MNRAS, 253, 31P
Balmaverde, B., Gilli, R., Mignoli, M., et al. 2017, A&A, 606, A23
Bañados, E., Venemans, B., Walter, F., et al. 2013, ApJ, 773, 178
Bañados, E., Venemans, B. P., Decarli, R., et al. 2016, ApJS, 227, 11
Bertin, E. 2006, in ASP Conf. Ser. 351, Astronomical Data Analysis Software and Systems XV, ed. C. Gabriel et al. (San Francisco, CA: ASP), 112
Bertin, E., & Arnouts, S. 1996, A&AS, 117, 393
Bertin, E., Mellier, Y., Radovich, M., et al. 2002, in ASP Conf. Ser. 281, Astronomical Data Analysis Software and Systems XI, ed. D. A. Bohlender, D. Durand, & T. H. Handley (San Francisco, CA: ASP), 228
Bowler, R. A. A., Dunlop, J. S., McLure, R. J., et al. 2015, MNRAS, 452, 1817
Bradley, L., Sipőcz, B., Robitaille, T., et al. 2021, astropy/photutils: 1.1.0, v1.1.0, Zenodo, doi: 10.5281/zenodo.4624996
Brammer, G. 2021, eazy-py, v0.5.2, Zenodo, doi:10.5281/zenodo.5012704
Brammer, G. B., van Dokkum, P. G., & Coppi, P. 2008, ApJ, 686, 1503
Chabrier, G., Baraffe, I., Allard, F., & Hauschildt, P. 2000, ApJ, 542, 464
Chambers, K. C., Magnier, E. A., Metcalfe, N., et al. 2016, arXiv:1612.05560
Champagne, J. B., Casey, C. M., Finkelstein, S. L., et al. 2023, ApJ, 952, 99
Champagne, J. B., Decarli, R., Casey, C. M., et al. 2018, ApJ, 867, 153
Chiang, Y.-K., Overzier, R., & Gebhardt, K. 2013, ApJ, 779, 127
Chiang, Y.-K., Overzier, R. A., Gebhardt, K., & Henriques, B. 2017, ApJL, 844, L23
Conroy, C., & Gunn, J. E. 2010, ApJ, 712, 833
Conroy, C., Gunn, J. E., & White, M. 2009, ApJ, 699, 486
Costa, T., Sijacki, D., Trenti, M., & Haehnelt, M. G. 2014, MNRAS, 439, 2146
Croom, S. M., Boyle, B. J., Shanks, T., et al. 2005, MNRAS, 356, 415
da Ângela, J., Outram, P. J., Shanks, T., et al. 2005, MNRAS, 360, 1040
De Rosa, G., Decarli, R., Walter, F., et al. 2011, ApJ, 739, 56
Di Matteo, T., Khandai, N., DeGraf, C., et al. 2012, ApJL, 745, L29
Di Matteo, T., Springel, V., & Hernquist, L. 2005, in Growing Black Holes: Accretion in a Cosmological Context, ed. A. Merloni, S. Nayakshin, & R. A. Sunyaev (Berlin: Springer), 340
Eftekharzadeh, S., Myers, A. D., White, M., et al. 2015, MNRAS, 453, 2779
Eilers, A.-C., Simcoe, R. A., Yue, M., et al. 2023, ApJ, 950, 68
Fan, X., Bañados, E., & Simcoe, R. A. 2023, ARA&A, 61, 373
Fan, X., Strauss, M. A., Becker, R. H., et al. 2006, AJ, 132, 117
Giallongo, E., Ragazzoni, R., Grazian, A., et al. 2008, A&A, 482, 349
Goto, T., Utsumi, Y., Kikuta, S., et al. 2017, MNRAS, 470, L117
Gunn, J. E., & Peterson, B. A. 1965, ApJ, 142, 1633
Haehnelt, M. G., & Rees, M. J. 1993, MNRAS, 263, 168
Harikane, Y., Ouchi, M., Ono, Y., et al. 2016, ApJ, 821, 123
Harris, C. R., Millman, K. J., van der Walt, S. J., et al. 2020, Natur, 585, 357
Hunter, J. D. 2007, CSE, 9, 90
Ilbert, O., Arnouts, S., McCracken, H. J., et al. 2006, A&A, 457, 841
Ilbert, O., Capak, P., Salvato, M., et al. 2009, ApJ, 690, 1236
Inayoshi, K., Visbal, E., & Haiman, Z. 2020, ARA&A, 58, 27
Inoue, A. K., Shimizu, I., Iwata, I., & Tanaka, M. 2014, MNRAS, 442, 1805
Jiang, L., McGreer, I. D., Fan, X., et al. 2016, ApJ, 833, 222
Kashikawa, N., Kitayama, T., Doi, M., et al. 2007, ApJ, 663, 765
Kashino, D., Lilly, S. J., Matthee, J., et al. 2023, ApJ, 950, 66
Kim, S., Stiavelli, M., Trenti, M., et al. 2009, ApJ, 695, 809
Landy, S. D., & Szalay, A. S. 1993, ApJ, 412, 64
Lee, K.-S., Giavalisco, M., Gnedin, O. Y., et al. 2006, ApJ, 642, 63
Lee-Brown, D. B., Rudnick, G. H., Momcheva, I. G., et al. 2017, ApJ, 844, 43
Lukić, Z., Heitmann, K., Habib, S., Bashinsky, S., & Ricker, P. M. 2007, ApJ, 671, 1160
Marley, M. S., Saumon, D., Visscher, C., et al. 2021, ApJ, 920, 85
Matthee, J., Mackenzie, R., Simcoe, R. A., et al. 2023, ApJ, 950, 67
Mazzucchelli, C., Bañados, E., Decarli, R., et al. 2017, ApJ, 834, 83
McKinney, W. 2010, in Proc. 9th Python in Science Conf., ed. S. van der Walt & J. Millman, 56
McKinney, W. 2011, Python for High Performance and Scientific Computing, 14, 1
McLure, R. J., Cirasuolo, M., Dunlop, J. S., Foucaud, S., & Almaini, O. 2009, MNRAS, 395, 2196
Meyer, R. A., Decarli, R., Walter, F., et al. 2022, ApJ, 927, 141
Mignoli, M., Gilli, R., Decarli, R., et al. 2020, A&A, 642, L1
Mo, H. J., & White, S. D. M. 2002, MNRAS, 336, 112
Morselli, L., Mignoli, M., Gilli, R., et al. 2014, A&A, 568, A1
Nantais, J. B., Muzzin, A., van der Burg, R. F. J., et al. 2017, MNRAS, 465, L104
Ota, K., Venemans, B. P., Taniguchi, Y., et al. 2018, ApJ, 856, 109
Overzier, R. A. 2016, A&ARv, 24, 14
Overzier, R. A., Bouwens, R. J., Illingworth, G. D., & Franx, M. 2006, ApJL, 648, L5
Overzier, R. A., Guo, Q., Kauffmann, G., et al. 2009, MNRAS, 394, 577
Pickles, A. J. 1998, PASP, 110, 863
Puget, P., Stadler, E., Doyon, R., et al. 2004, Proc. SPIE, 5492, 978
Roche, N., & Eales, S. A. 1999, MNRAS, 307, 703
Romano-Diaz, E., Shlosman, I., Trenti, M., & Hoffman, Y. 2011, ApJ, 736, 66
Scannapieco, E., & Oh, S. P. 2004, ApJ, 608, 62
Simpson, C., Mortlock, D., Warren, S., et al. 2014, MNRAS, 442, 3454
Sinha, M., & Garrison, L. H. 2020, MNRAS, 491, 3022
Skrutskie, M. F., Cutri, R. M., Stiening, R., et al. 2006, AJ, 131, 1163
Speziali, R., Di Paola, A., Giallongo, E., et al. 2008, Proc. SPIE, 7014, 70144T
Springel, V., White, S. D. M., Jenkins, A., et al. 2005, Natur, 435, 629
Stanway, E. R., Bunker, A. J., & McMahon, R. G. 2003, MNRAS, 342, 439
Stiavelli, M., Djorgovski, S. G., Pavlovsky, C., et al. 2005, ApJL, 622, L1
Utsumi, Y., Goto, T., Kashikawa, N., et al. 2010, ApJ, 721, 1680
van Dokkum, P. G. 2001, PASP, 113, 1420
Venemans, B. P., Findlay, J. R., Sutherland, W. J., et al. 2013, ApJ, 779, 24
Virtanen, P., Gommers, R., Oliphant, T. E., et al. 2020, NatMe, 17, 261
Volonteri, M., Habouzit, M., & Colpi, M. 2021, NatRP, 3, 732
Wang, F., Wang, R., Fan, X., et al. 2019a, ApJ, 880, 2
Wang, F., Yang, J., Fan, X., et al. 2019b, ApJ, 884, 30
Wang, F., Yang, J., Hennawi, J. F., et al. 2023, ApJL, 951, L4
Wang, Y., Brunner, R. J., & Dolence, J. C. 2013, MNRAS, 432, 1961
Weaver, J. R., Kauffmann, O. B., Ilbert, O., et al. 2022, ApJS, 258, 11
Whitler, L., Stark, D. P., Endsley, R., et al. 2024, MNRAS, 529, 855
Willott, C. J., Percival, W. J., McLure, R. J., et al. 2005, ApJ, 626, 657
Wu, X.-B., Wang, F., Fan, X., et al. 2015, Natur, 518, 512
Yang, J., Wang, F., Fan, X., et al. 2019, AJ, 157, 236
Yang, J., Wang, F., Fan, X., et al. 2021, ApJ, 923, 262
Zonca, A., Singer, L., Lenz, D., et al. 2019, JOSS, 4, 1298